

Simulation and test of the SLEGS TOF spectrometer at SSRF*

Kai-Jie Chen (<https://orcid.org/0000-0002-0007-913X>),^{1,2} Long-Xiang Liu,³
Zi-Rui Hao,^{4,2} Yu-Gang Ma (<https://orcid.org/0000-0002-0233-9900>),^{5,†}

Hong-Wei Wang (<https://orcid.org/0000-0002-8178-0605>),^{3,4,2,‡} Gong-Tao Fan,^{3,4,2} Xi-Guang Cao,^{3,4,2} Hang-Hua Xu,³
Yi-Fei Niu (<https://orcid.org/0000-0003-1029-1887>),⁶ Xin-Xiang Li (<https://orcid.org/0000-0002-4896-8200>),^{7,4,2}
Xin-Rong Hu (<https://orcid.org/0000-0002-1677-9528>),^{4,2} Yu-Xuan Yang,^{2,8} Sheng Jin,^{4,2} and Pan Kuang^{4,2}

¹School of Physical Science and Technology, ShanghaiTech University, Shanghai 201210, China

²Shanghai Institute of Applied Physics, Chinese Academy of Sciences, Shanghai 201800, China

³Shanghai Advanced Research Institute, Chinese Academy of Sciences, Shanghai 201210, China

⁴University of Chinese Academy of Science, Beijing 100080, China

⁵Key Laboratory of Nuclear Physics and Ion-beam Application (MOE),

Institute of Modern Physics, Fudan University, Shanghai 200433, China

⁶School of Nuclear Science and Technology, Lanzhou University, Lanzhou 730000, China

⁷School of Nuclear Science and Technology, University of South China, Hengyang 421001, China

⁸School of Physics and Microelectronics, Zhengzhou University, Zhengzhou 450052, China

The Shanghai Laser Electron Gamma Source (SLEGS) is a powerful tool for exploring photonuclear physics, such as giant dipole resonance (GDR) and pygmy dipole resonance (PDR), which are the main mechanisms of collective nuclear motion. The goal of the SLEGS neutron time-of-flight (TOF) spectrometer is to measure GDR and specific nuclear structures in the energy region above the neutron threshold. The SLEGS TOF spectrometer was designed to hold 20 sets of EJ301 and LaBr₃ detectors. Geant4 was used to simulate the efficiency of each detector and the entire spectrometer, which provides a reference for the selection of detectors and layout of the SLEGS TOF spectrometer. Under the events of ²⁰⁸Pb, implementations of coincidence and time-of-flight technology for complex experiments are available; thus, γ and neutron decay events can be separated. The performance of SLEGS TOF spectrometer was systematically evaluated using offline experiments, in which the time resolution reached approximately 0.9 ns.

Keywords: SLEGS, Time-of-flight, Photoneutron nuclear reaction

I. INTRODUCTION

The Shanghai Laser Electron Gamma Source (SLEGS), which is a high-intensity γ -ray beamline based on laser Compton scattering (LCS) between 3.5 GeV, 200 mA relativistic electron bunches in the storage ring of the Shanghai Synchrotron Radiation Facility (SSRF) [1], and 10.64 μ m 100 W CO₂ laser, was commissioned at the beginning of 2022 [2, 3]. Owing to the innovative design of the interaction chamber [4] and dual collimation system [5, 6], SLEGS can operate in two modes to obtain tunable high-intensity Compton spectrum of γ -rays from 0.66 MeV to 21.7 MeV with a full-spectrum flux of 10^5 - 10^7 photons/s.

In addition, the CO₂ laser of the SLEGS can be operated in pulse mode with an adjustable laser interval and pulse width, for example, a 1 ms laser interval and 100 μ s pulse width at 10 W with a 10% duty cycle. In the SSRF top-up and continuous-wave laser modes, the maximum beam flux is obtained, which is suitable for small cross-section measurements with some targets. More detailed information concerning the interaction chamber, dual collimation system, flux at-

tenuator, and commissioning results has been published elsewhere [4–7].

As a nuclear physics experimental platform, SLEGS aims at basic and applied research related to photonuclear reactions ranging from photon excitation to photon disintegration, such as nuclear resonance fluorescence, neutron production, and charged particle production [3, 8–10]. To achieve the above basic research goals, SLEGS has been equipped with four types of experimental spectrometers: gamma nuclear resonance fluorescence (NRF), neutron flat-efficiency detector (FED) [11], TOF, and light charged-particle (LCP) spectrometers, where both TOF and FED spectrometers can be used for (γ, n) reaction measurements. (γ, n) reactions have been measured using the ring-ratio method [12, 13] and direct neutron multiplicity sorting method [11, 14] using an FED spectrometer. However, FED spectrometers fail to measure neutron energy; therefore, it cannot acquire information on neutron energy. Similar to other TOF measurements [15–17], SLEGS TOF spectrometers can measure fast neutron energy, which is necessary for the study of isovector giant dipole resonance (IVGDR) [18–21]. Because of the limitations of the construction and development of gamma sources, measurements of GDR based on photon sources have been restricted over the past 20 years [22].

The γ -rays of SLEGS are currently available for experimental research on IVGDR. The SLEGS TOF spectrometer, which serves the same purpose as the ELIGANT [23, 24] at Extreme Light Infrastructure–Nuclear Physics (ELI-NP), was designed to measure the γ -rays and neutron radiation emitted

* This work was supported by the National Natural Science Foundation of China(Nos. 12275338, 12005280, 11905274 and 11875311), the Key Laboratory of Nuclear Data foundation (JCKY2022201C152), National key research and development program(No. 2022YFA1602404), the Strategic Priority Research Program of the CAS (No. XDB34030000).

† Corresponding author, mayugang@fudan.edu.cn

‡ Corresponding author, wanghongwei@zjlab.org.cn

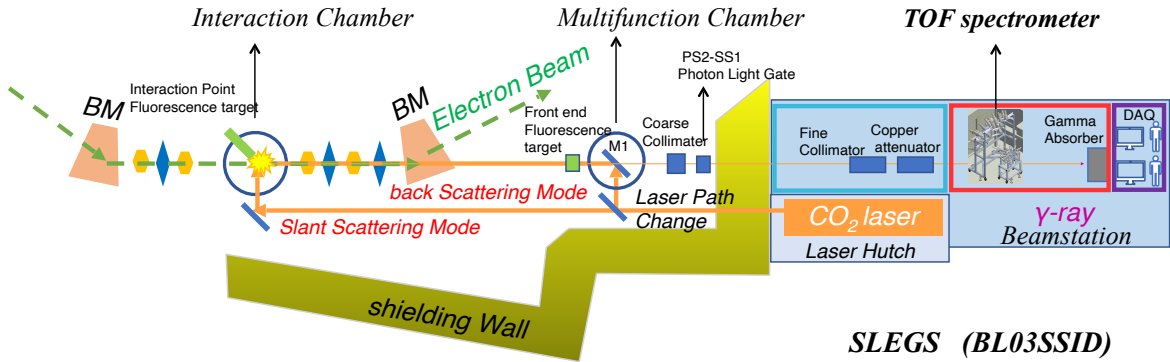


Fig. 1. (Color online) A schematic layout of the SLEGS beamline.

Table 1. Related parameters of the SLEGS TOF spectrometer.

Detector	Number	Material	Density (g/cm ³)	Distance (cm)	Diameter (inches)	Thickness (inches)
LaBr ₃	8-20	LaBr ₃	5.10	30	3	4
EJ301	20	xylene	0.86	150	5	2

during the decay of nuclear collective states. Therefore, the SLEGS TOF spectrometer has two main parts for γ -ray and neutron detection. In addition, two mechanical supports were designed to hold 20×EJ301 and (8 – 20)×LaBr₃ detectors, as shown in Fig. 2.

In this study, we focused on the simulation, calibration, and other tests of the SLEGS TOF spectrometer, which plays an essential role in photo-neutron measurements.

II. SIMULATION OF THE SLEGS TOF SPECTROMETER

All simulations were based on Geant4 version 11.0.1 [25]. Various influencing factors were considered, and different interaction models were used for accurate simulations. For neutron interactions, QGSP_BERT_HP at neutrons \leq 20 MeV used high-precision neutron models and cross-sections to describe elastic and inelastic scattering, capture, and fission. A G4NDL database was required for this physics list. Moreover, RadioactiveDecay was activated.

For the electromagnetic interactions, QGSP_BERT_HP was used as the default EM constructor. The emstandard_opt3, which is more suitable for the simulation of SLEGS TOF designed for any application, required a higher accuracy of electrons, hadrons, and ion tracking without a magnetic field. Therefore, emstandard_opt3 replaced the default EM constructor in the QGSP_BERT_HP. In this case, e^+e^- pair production was implemented using the BetheHeitler model with an LPM effect at high energies, and Compton scattering was implemented using the Klein-Nishina model. The photon-electric effect and Rayleigh scattering were both handled by the Livermore models. Different particle generators were constructed for different simulation purposes, such as monochromatic and isotropic gamma and neutron point sources. The geometries of the detectors and

other parts were constructed consistently with the reality. The material properties of the detectors are listed in Table 1.

A. The SLEGS TOF spectrometer

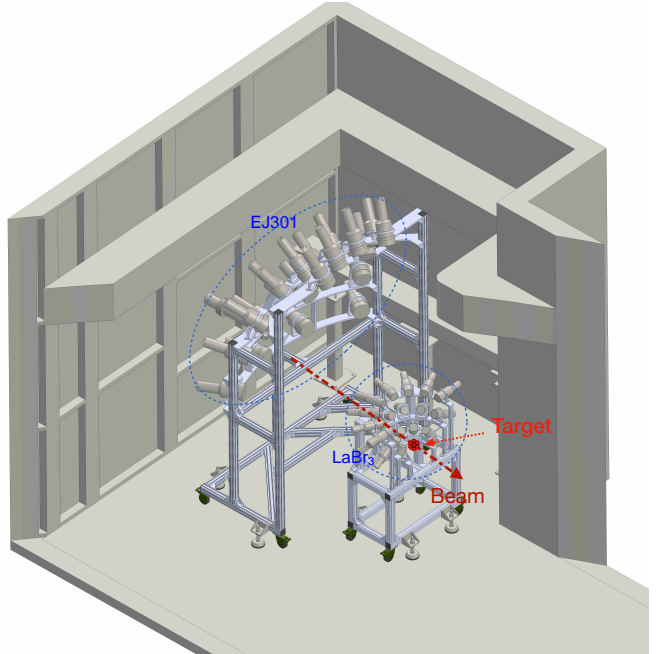


Fig. 2. (Color online) Layout of SLEGS TOF spectrometer. The LaBr₃ and EJ301 detectors (with two blue dotted ellipses) were placed at 30 cm and 150 cm from the target, respectively, all in the backward direction of the beam (with a red arrow).

This section presents the construction of a complete

SLEGS TOF detector array model, considering the factors that affect the measurement. $(8 - 20) \times \text{LaBr}_3$ and $20 \times \text{EJ301}$ were placed 30 cm and 150 cm from the target. The spectrometer was placed close to the beam exit, far from the beam dump, and reserved for beam-spot monitoring, and an external collimator was placed at the front of the experimental hutch. All detectors were placed in the backward hemisphere to reduce the background, as discussed in Sect. II D. Shielding, attenuators, and PMTs were also considered.

B. Gamma detectors efficiency

For GDR measurements with small cross-sections, the detection efficiency is an important consideration, which directly determines the design of the experimental scheme and beam time. Gamma detectors are used to capture the γ -rays emitted during the decay of collective states. In particular, when the SSRF is in the top-up mode and the laser is in continuous output mode, LaBr_3 must provide the starting time of TOF measurement by detecting de-excitation of γ -rays due to neutron decay.

Therefore, the gamma detectors must be fast and large enough to completely stop the γ -rays produced by high-energy beams and close to the target for high absolute efficiencies and short time delays. A large-volume scintillator was selected because of its high efficiency, large size, and ease of maintenance. Considering its cost, LaBr_3 detectors, which are used for beam monitoring and diagnosis, were chosen for gamma detection. Larger diameter detectors significantly increase the solid angle of coverage, while also implying greater sensitivity to the beam background. Crystals with a diameter of 3 in are easily available. In [26], the characteristics of energy resolution, pulse shape, and time response of large volume LaBr_3 are discussed. The performance of LaBr_3 with different thicknesses was simulated using attenuators and shielding. Fig. 3(a) shows the full energy peak intrinsic efficiencies of single LaBr_3 crystals of different sizes at γ -ray energies below 22 MeV.

The simulation results showed that a larger detector volume can provide higher intrinsic efficiencies. For a good balance between cost and γ -ray efficiency, crystals with 3 in \times 4 in LaBr_3 were used as the γ -ray detectors in the SLEGS TOF spectrometer. Figure 3(b) shows the full energy peak absolute efficiencies of the $20 \times \text{LaBr}_3$ arrays with respect to different γ -ray energies. In this energy region (1 to 22 MeV), the full energy peak absolute efficiencies of the LaBr_3 array decreased rapidly with increasing γ energy. It can be seen that the full energy peak absolute efficiencies were less than 0.5% for the γ -ray energy higher than 10 MeV. From the results of the peak-to-total ratio shown in Fig. 3(c), it can be seen that to obtain one 9 MeV γ -ray accumulated in the full energy peak, the detectors must capture at least approximately 30 γ -rays on average.

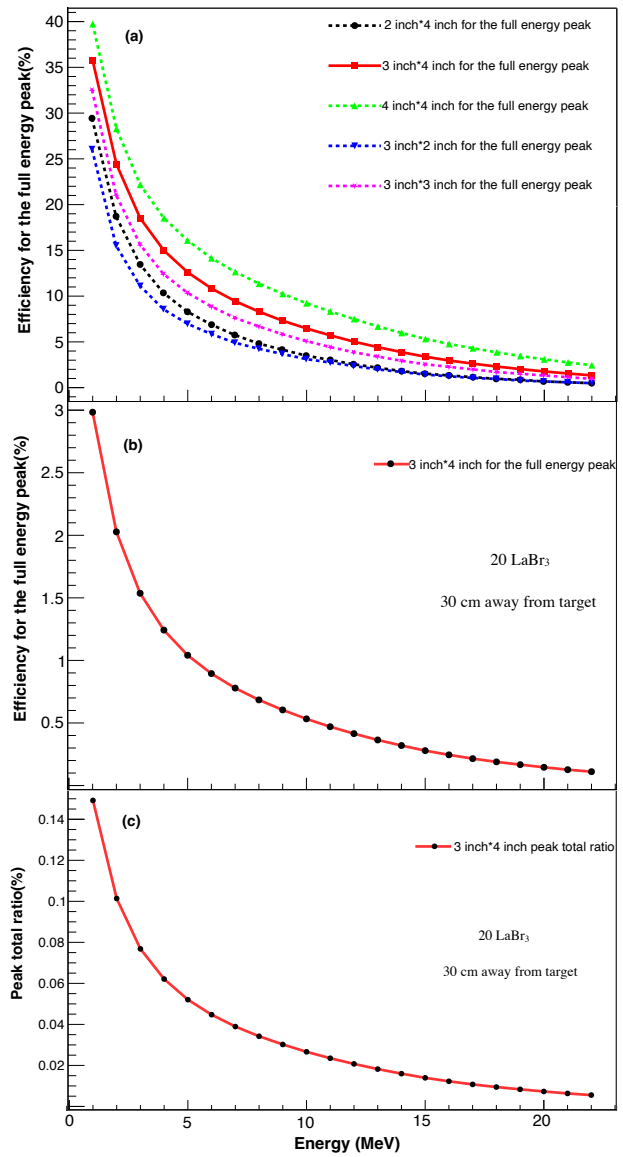


Fig. 3. (Color online) (a) Full-energy peak intrinsic efficiencies of a single detector as a function of incident γ -ray energies simulated for a LaBr_3 crystal with different sizes (see legend), (b) full-energy peak absolute efficiencies of $20 \times \text{LaBr}_3$ with 3 in \times 4 in, and (c) peak total ratio of $20 \times \text{LaBr}_3$. Here, the monotonous energy point source generators were used, with γ -ray energies from 1 MeV to 22 MeV.

C. Neutron detectors efficiency

Neutron detection and background control are important for nuclear astrophysics and technology applications [27–30]. In the IVGDR, decay neutrons may be also emitted, which can normally be measured using the TOF technique. The uncertainty in the distance and time resolution of the detector determines the accuracy of the reconstructed neutron energy. In general, a longer neutron flight distance is beneficial for reducing distance uncertainty. However, the solid angle covered by the detector is inversely proportional to the square

of the distance, resulting in lower absolute efficiency. Therefore, the time response and the efficiency of the detector are important reference factors. Organic liquid scintillation detectors are commonly used for the detection of fast neutrons. Owing to the abundance of hydrogen atoms in scintillators, the deposited energy of neutrons via recoiling protons mostly excites the electrons of scintillator molecules, and their de-excitation leads to the emission of optical photons. The classic liquid scintillators BC501A, EJ301, and NE213 have been used in different arrays such as ENDA and ELINPGIANT-GN[31–33].

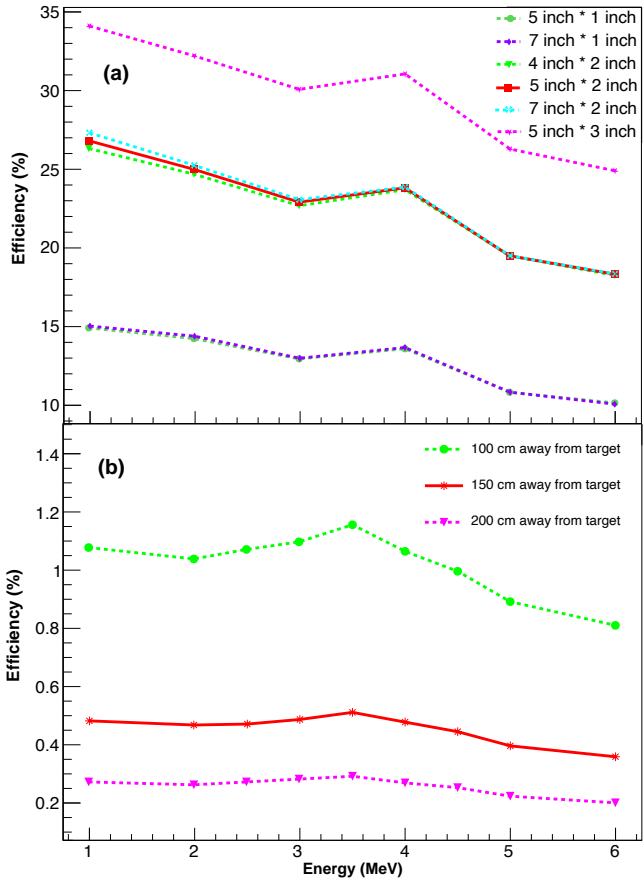


Fig. 4. (Color online) (a) Simulated detector intrinsic efficiencies for an EJ301 scintillator detector of different sizes of 1 MeV to 6 MeV fast neutrons and (b) 20×EJ301 array absolute efficiencies in three positions: 100, 150, and 200 cm from target. The mono-energetic isotropic neutron point source generators were used.

However, EJ301 has been adopted as a substitute for BC501A, which exhibits almost the same performance [34, 35] for neutron detection. Figure 4(a) shows the detector intrinsic efficiencies simulated for EJ301 scintillator detectors of different sizes of 1 to 6 MeV fast neutrons. To increase the solid angle that the neutron detectors covered, 20 EJ301 detectors of 5 in in diameter were placed 150 cm from the target that suffered from an experimental hutch size restriction, which was irrevocable. A length of 2 in was considered a good balance for efficiency, pulse shape discrimination

(PSD), neutron flight distance uncertainty, and cost.

Similarly, the neutron detection absolute efficiencies of 20 EJ301 arrays placed 100, 150, and 200 cm from the target were also simulated, and the results are shown in Fig. 4(b). It should be emphasized that the variation at 4 MeV corresponded to the scattering cross-section of carbon [36]. The kinetic energy of a neutron is proportional to the square of its velocity, which can be determined by dividing its flight distance by its flight time. Thus, the neutron energy resolution was determined by two factors: uncertainty of the neutron flight distance and uncertainty of the neutron flight time. For the former, the detector length and distance between the detector and target were determined together. For EJ301 with a thickness of 2 in, the uncertainties of the neutron flight paths were 2.43 %, 1.64 %, and 1.23 % at three different distances of SI100, SI150, and SI200 cm, respectively. Obviously, longer flight paths resulted in more accurate neutron energy measurements, whereas the absolute efficiencies were reduced considerably, as shown in Fig. 4(b). The uncertainty of neutron flight time is discussed in Sect. III D.

D. Background contribution

Figure 5(a) shows the γ rays that hit the Pb target and produced the aforementioned background. The most striking result was that the emitted background did not scale with the target thickness. Moreover, particle trash multiple scattering was evident. However, because the distance from the LaBr₃ detectors was greater than 3 m, the absolute efficiency was extremely low; therefore, its influence was negligible. It is important to note that the mechanisms involved in high-energy γ -rays were mainly Compton scattering and pair production, and the cross sections were several orders of magnitude higher than that of GDR. The simulation results revealed that when 9 MeV γ -rays interacted with a 1 mm lead target, the electron pair production process exceeded 70%, and the Compton scattering was close to 30%. Based on the simulation of the background components, the source of the background mainly came from γ -rays, whereas most of the charged particles, such as electrons and positrons, were absorbed by the shieldings and attenuators of the detector.

Figure 5(b) shows the angular distribution of the background. The background emission was clearly forward; therefore, the detectors were placed in the rear-angle direction. In particular, in the 90° direction, the minimum was reached owing to the shadow effect and the self-absorption of the finite-size target. Figure 5(c) compares the background spectra simulated in different directions for 9 MeV γ -rays focused on a 1 mm Pb target, considering the hutch shielding wall and particle trash.

E. Pb target simulation

Finally, the GDR of the Pb targets was used for the validation and benchmarking of the code and the feasibility of co-incident measurement. The experimental data for GDR[22]

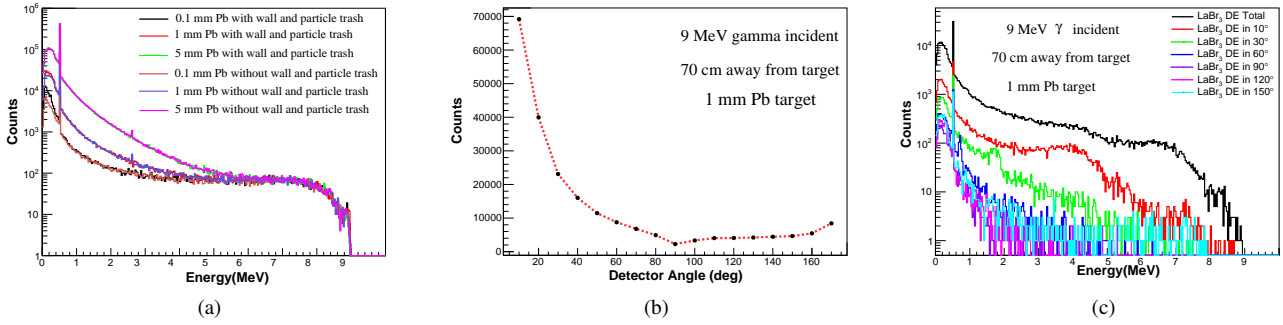


Fig. 5. (Color online) (a) Background energy spectra simulated for $20 \times \text{LaBr}_3$ detectors after emission of 9 MeV γ -rays into 0.1, 1, and 5 mm Pb targets, where the influence of experiment hutch shielding wall and particle trash were considered for some cases(see legend), (b) angular distribution of background simulated for $17 \times \text{LaBr}_3$ detectors placed 70 cm from target, 9 MeV γ -rays (10^8) focused on a 1 mm Pb target, and (c) energy spectra of LaBr_3 simulated at different directions, with conditions shown in the panel.

were fewer than those for calculations based on theoretical models [21, 37–41]. The reliability of the SLEGS TOF spectrometer was verified using the GDR experimental data in ^{208}Pb .

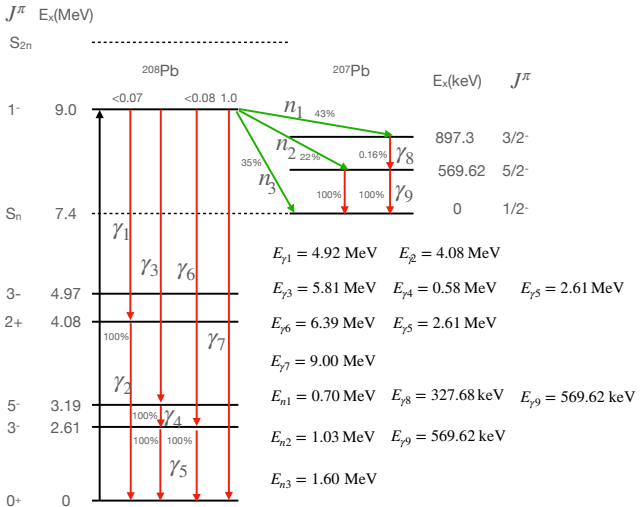


Fig. 6. Partial decay scheme of ^{208}Pb .

To prove the feasibility of measuring the GDR using the SLEGS TOF spectrometer, a specific event generator in ^{208}Pb that encompassed seven channels of probabilities of decay[22, 32] was required: P1, P2, P3, and P4 cases were pure gamma decays, accounting for 2%, whereas the dominant decay was by emitting neutrons. In particular, the P6 and P7 cases were suitable for measurement with SLEGS TOF spectrometer, where the simultaneously emitted γ -rays only required approximately 1 ns to travel through a flight distance of 30 cm, whereas the neutrons travel through a flight distance of 150 cm to improve the accuracy of neutron energy measurement. The time the EJ301 liquid scintillation detectors started determining neutron energy was the time at which the LaBr_3 detector placed at 30 cm captured γ -rays used as. The seven different channel probabilities are sum-

marized in Table 2 and are shown in Fig. 6. Based on the decay scheme, a generator comprising an isotropic neutron source and γ source was coded.

Table 2. Parameters of different decay channels[22, 32].

Case	Particle	Energy (MeV)	Branch ratio	Probability
P1	γ	9.00	93.46%	
P2	γ_1	4.92	1.87%	
	γ_2	4.08		
P3	γ_6	6.39	3.74%	2%
	γ_5	2.61		
	γ_3	5.81		
P4	γ_4	0.58	0.93%	
	γ_5	2.61		
P5	n_3	1.60	35%	
P6	n_2	1.03	22%	
	γ_9	0.56962		98%
	n_1	0.70		
P7	γ_8	0.32768	43%	
	γ_9	0.56962		

The time spectra of the LaBr_3 detectors without any conditions are shown in Fig. 7(a). An obvious γ -ray peak and three neutron peaks can be observed in the figure, where the γ -ray peak consists of pure gamma decay and γ -rays emitted concomitantly by neutron decay. For the three neutron peaks, the neutron decays corresponding to 1.6, 1.03, and 0.7 MeV, were magnified and marked in the inset. The energy spectra when different time gates were used are shown in Fig. 7(b). The separated prompt γ -ray peaks, delayed neutron events, and some background γ -rays can be clearly observed. The branching ratio was obtained from the relative intensity of the γ -ray peak, and the corresponding energy level was obtained from the energy of the full energy peak or escaped peak under the appropriate time gate. In particular, the energy spectrum of LaBr_3 shown in Fig. 8, with a 0–2 ns self-prompt time gate and γ -ray peaks, is marked.

Similarly, the time spectrum of EJ301 neutron detector without a time gate is shown in Fig. 9(a), whereas the energy spectra with different time gates are shown in Fig. 9(b).

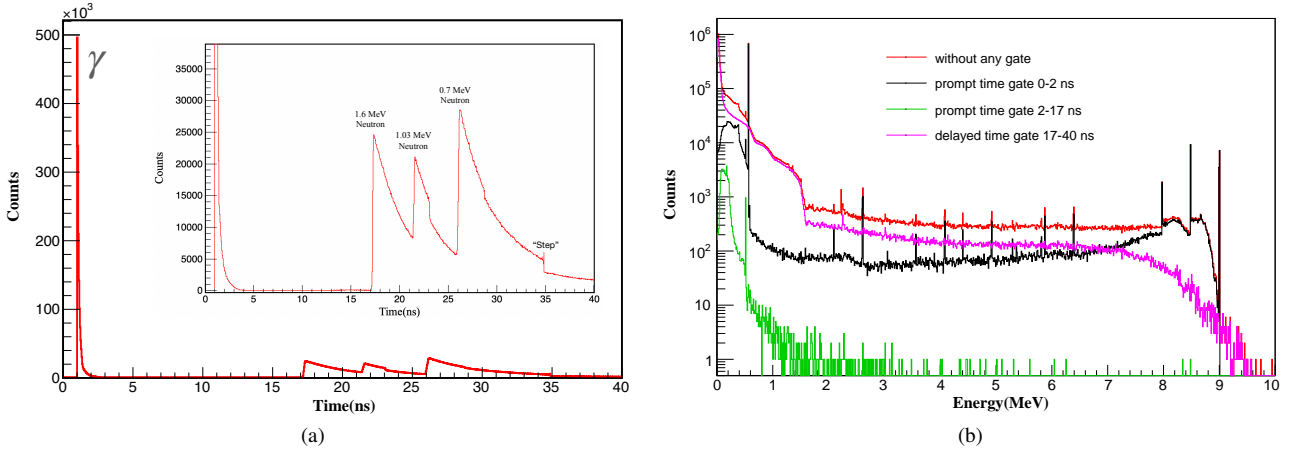


Fig. 7. (Color online) (a) Time-of-flight spectrum of LaBr₃ without any gates. Three neutron peaks are magnified and their energies are marked in the inset. (b) Energy spectra of LaBr₃ with some different time gates. The black lines represent the pure gamma decay and γ -rays accompanied by neutron decay. The green line represents the background. The pink lines represent the neutron events and associated background. The resolution of the LaBr₃ detectors was not considered.

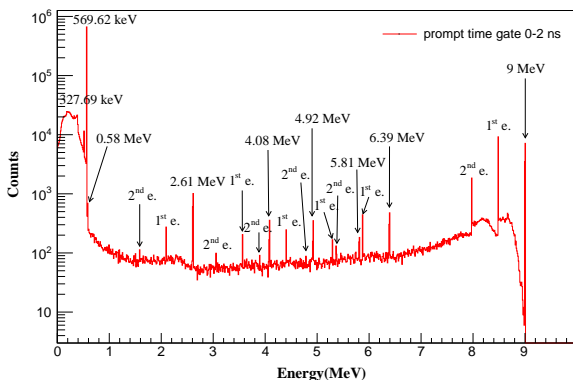


Fig. 8. Energy spectrum of LaBr₃ with a 0–2 ns self-prompt time gate condition. The resolution of LaBr₃ was not considered.

As expected, a clear separation of the neutrons decaying into different energy levels was achieved.

F. Coincidence simulation results

Using TOF technology for measuring the neutron energy, the energy resolution only reached an order of 10%. When the incident energy exceeded the double-neutron separation energy, more reaction channels were opened. It was impossible to identify individual exclusive decays of GDR in heavy nuclei solely through neutron detection because of the limited energy resolution and dense-level schemes of residual nuclei. Therefore, the practicality of the coincidence technology implemented between different detectors was studied. The fold event distributions of the LaBr₃ detectors, EJ301 detectors, and entire SLEGS TOF spectrometer are shown in Fig. 10. A fold event was a similar event recorded by multiple detectors.

Most of the events were single. The multiple events detected by the LaBr₃ detectors were significantly more than those detected by the EJ301 detectors because they were placed adjacent to each other and the generators involved multiple gamma particle emissions from GDR to low-lying states. In contrast, the EJ301 detectors were more dispersed because of limited budget. Multiple events were easily applied to select interesting and correlated events. The $\gamma - \gamma$ coincidence energy spectrum for LaBr₃ is shown in Fig. 11(a) corresponding to multiple-step decays, such as the P2, P3, and P7 cases. In particular, an additional condition $E_{\gamma 1} + E_{\gamma 2} = 9$ MeV was applied to select two-step pure gamma decays, and the energy spectrum is shown in Fig. 11(b). The energy spectra of coincidence between γ -rays detected by LaBr₃ and neutrons detected by EJ301 are shown in Fig. 12(a), which corresponded to the multistep decay of the P6 and P7 cases. These cases were the initial experiment of interest for the SLEGS TOF spectrometer. Because the start time signal was obtained by the LaBr₃ detectors, which was independent of the time signal from the beam, the complexity of the experiment was significantly reduced. In conclusion, it is feasible to select interested decay channels using the coincidence techniques.

III. EXPERIMENT TEST RESULTS

A. Data acquisition system

The location of each component of SLEGS is shown in Fig. 1. The SLEGS TOF was installed in the experimental hutch located between the laser and data acquisition hutches. In the experimental hutch, various spectrometers were used to conduct the experiment using various methods. Some computers, which were connected to the laser system, beamline modulation system, and data acquisition plug-in via optical fiber controlled the beamline and acquired the spectrometer data in the

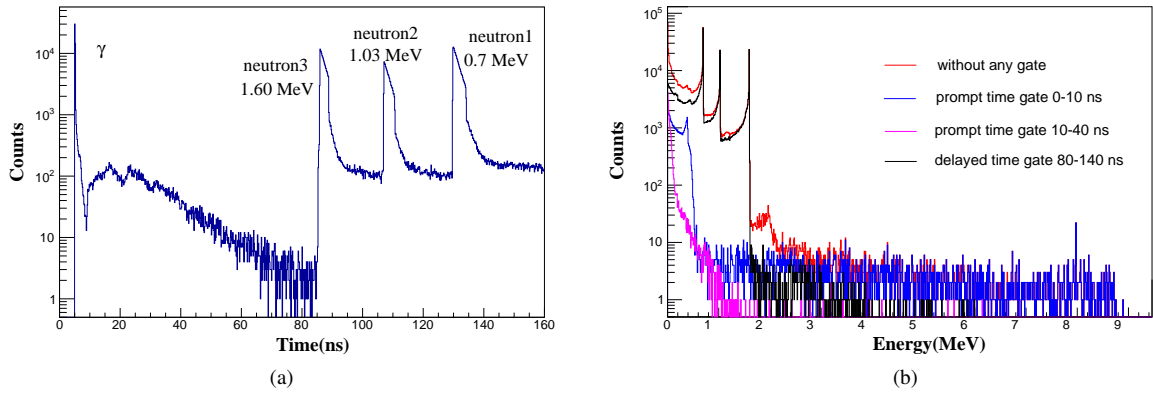


Fig. 9. (Color online) (a) Time-of-flight spectrum of EJ301 without a gate, and (b) energy spectra of EJ301 with different time gates. The black lines indicate the neutron events. The blue lines represent the pure gamma decay and γ -rays accompanied by neutron decay, and the pink line represents the background. The resolution of the detectors was not considered.

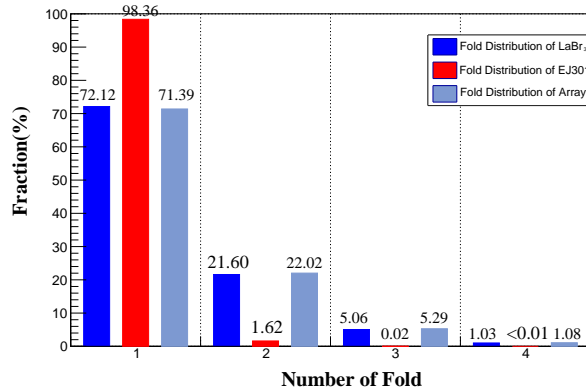


Fig. 10. (Color online) Fold event distributions for LaBr₃, EJ301, and entire SLEGS TOF spectrometer.

data acquisition (DAQ) hutch. The walls of all hutes consisted of concrete, polyethylene, and steel. A particle trash that was designed to absorb neutrons and γ -rays was built at the end of the experimental hutch. Therefore, an experimental hutch is suitable for neutron-production experiments. The entire SLEGS TOF spectrometer data-acquisition system consisted of two parts: high-voltage control modules and DAQ. The multiple N1470 boards[42], which had four output channels, each capable of up to 8 kV (with a resolution of ± 1 V), provided high voltage for LaBr₃ detectors. They were installed in a crate equipped with a compact UEP15–150 W[43] and a slot power supply, which provided five direct current (DC) voltages: (± 6 V 5 A, ± 12 V 3 A, ± 24 V 1.5 A). The power supply of the EJ301 detectors was provided by double A7030DN boards[44] installed in a SY5527LC universal multichannel power supply system[45]. Each A7030DN board had 12 channels, and the maximum output voltage and current reach 3 kV (with a resolution of 1 V) and 1 mA (with a resolution of 1 μ A), respectively. SY5527LC supported four slots with a maximum out-

put power of 200 W (with 220 Vac Mains) and 350 W (with 110 Vac Mains). In addition, the graphical control software and HiVoCS web tool performed remote operation via a host computer using TCP/IP communication protocol.

The signals from each detector were sent to the DAQ via 3 m, a bayonet Nill-Concelman (BNC) cable, which had similar specifications to avoid attenuation of different channel signals with a 50Ω impedance. The end of each cable was connected to a channel of digitizers via a BNC-micro coaxial connector (MCX) cable. Three CAEN V1730s digitizers provided 48 channels for $20 \times$ LaBr₃ and $20 \times$ EJ301, which were installed in an NV8020 versa module europa (VME) crate. V1730s [46] was a 1-unit wide VME 6U module, housing a 16-channel 14-bit 500 MS/s FLASH ADC waveform digitizer with software selectable 2 Vpp or 0.5 Vpp input dynamic range on single-ended MCX coaxial connectors. The DC offset was adjustable in the ± 1 V (@2 Vpp) or ± 0.25 V (@0.5 Vpp) range via a 16-bit digital-to-analog converter (DAC) in each channel. The module housed an optical link interface supporting a transfer rate of up to 80MB and provided a daisy chain capability. In addition to waveform recording firmware, CAEN provided four types of digital pulse processing(DPP) firmware: pulse shape discrimination (DPP-PSD), which is suitable for GDR measurement, pulse height analysis (DPP-PHA), zero length encoding (DPP-ZLEplus), and dynamic acquisition windows (DPP-DAW). Finally, a 40-m optical fiber was connected to a computer via an A3818 peripheral component interconnect express (PCIe)[47]. The computer was installed with CoMPASS readout software developed by CAEN, which can set parameters, display waveforms in real time, energy, timing, and PSD spectrum, and create root-format files.

B. Energy calibration, resolution, and efficiency

First, the existing $8 \times$ LaBr₃ energy and efficiency calibrations were carried out using the ⁶⁰Co and ¹³⁷Cs radiation

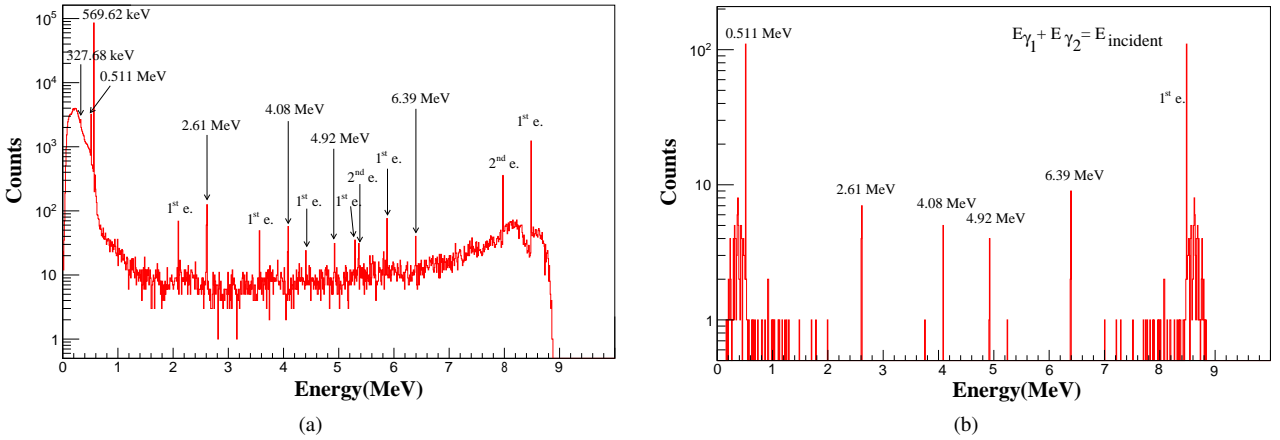


Fig. 11. (a) $\gamma - \gamma$ coincidence energy spectrum of LaBr_3 , and (b) energy spectrum of LaBr_3 with an additional gate of $E_{\gamma 1} + E_{\gamma 2} = 9 \text{ MeV}$. The resolution of the LaBr_3 detectors was not considered.

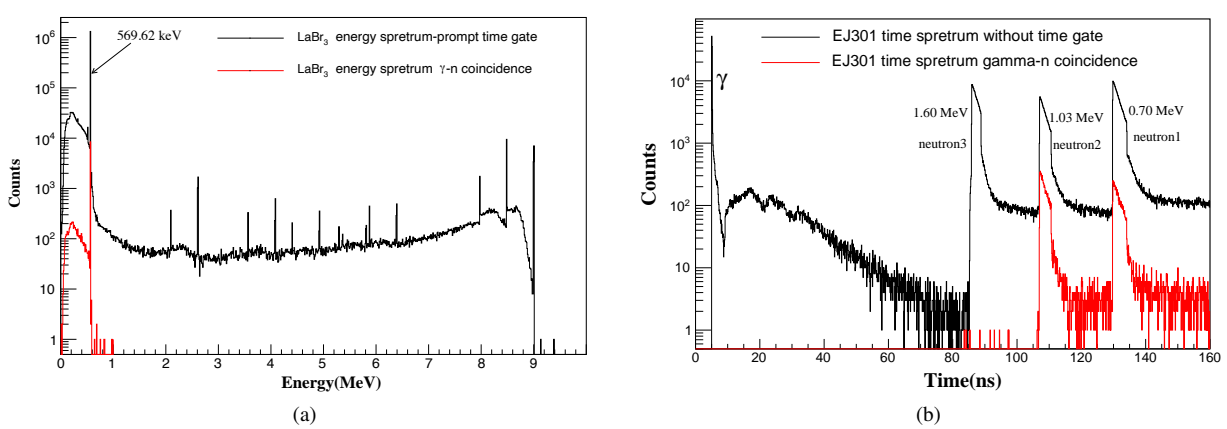


Fig. 12. Energy spectra of coincidence between γ -rays detected by LaBr_3 and neutrons detected by EJ301. In panel (a), coincidence γ -ray energy spectrum is shown as a red line, corresponding to γ_8 327.68 keV and γ_9 569.62 keV, whereas coincidence neutron time spectrum is shown in panel (b) as a red line, corresponding to n_2 1.03 MeV and n_3 1.60 MeV. The resolutions of the LaBr_3 and EJ301 detectors were not considered.

sources, and the results are presented in Table 3.

The full-energy peak efficiency comparison between the experimental data and the simulation is presented in Fig. 13, and it can be observed that they are almost consistent. Fig. 13 shows the average experimental values of the full-energy peak efficiencies of the eight LaBr_3 detectors. Based on the experiment with beam monitoring and diagnostics using LaBr_3 , the detection ranged from several hundred keV to 20 MeV. The detector measured synchrotron radiation up to approximately 300 MeV by reducing the high voltage. However, the detectors became blind when they faced high-flux gamma beams. In addition, because the LaBr_3 detectors had excellent energy resolution and measurement range of energy, we measured the direct γ decay from GDR to the ground state and the low-energy γ -rays emitted from the GDR decay to low-lying states.

The EJ301 liquid scintillation detector had poor energy resolution, unlike the LaBr_3 detector. Another difference was

in the scintillation response. The response of EJ301 was nearly linear with the deposited energy for particles that resulted in electron recoil, such as gamma interaction with the scintillator[48]. However, serious nonlinearities can emerge in nuclear recoil events, such as neutron interaction with a scintillator [49–51]. Apparently, separate energy calibrations of γ -rays and neutrons are necessary for EJ301 liquid scintillation detectors. In fact, EJ301 has been used to reconstruct neutron energy with TOF technology instead of directly determining energy via pulse height analysis (PHA) and analog-to-digital converters (ADC). Therefore, only γ -ray energy calibration of EJ301 was performed, and its time resolution is discussed in Sect. III D.

As liquid scintillation is rich in hydrogen atoms, the Compton scattering process was dominant in the interaction with γ -rays. A full-energy peak was not observed in the energy spectrum; therefore, it is not feasible for the fitting method to perform energy calibration. The experimental and simulated

Table 3. Parameters of eight LaBr₃ resolution and efficiency calibration

Model	HV (kV)	Threshold (keV)	¹³⁷ Cs 662 keV			⁶⁰ Co 1173 keV			⁶⁰ Co 1332 keV			Calibration parameters	
			FWHM	Resolution	Efficiency	FWHM	Resolution	Efficiency	FWHM	Resolution	Efficiency	K	B
A18782-1	733	260.19	3.60	2.98%	45.76%	4.95	2.32%	35.45%	5.18	2.14%	31.40%	5.514	-4.479
A18783-2	678	273.11	3.71	3.24%	45.19%	5.11	2.53%	34.46%	5.34	2.33%	30.98%	5.850	-7.686
A18784-3	652	259.28	3.70	3.09%	45.62%	5.04	2.38%	32.97%	5.24	2.19%	29.27%	5.598	-9.423
A18785-4	744	269.65	3.62	3.12%	45.15%	4.88	2.37%	34.97%	5.06	2.17%	31.37%	5.743	-6.016
A18786-5	638	245.84	3.65	2.87%	43.46%	4.90	2.18%	33.45%	5.06	1.98%	30.34%	5.247	-6.013
A18787-6	713	289.63	3.52	3.21%	44.17%	4.71	2.42%	34.55%	4.89	2.21%	30.57%	6.028	0.285
A18788-7	696	250.03	3.50	3.02%	47.17%	4.46	2.23%	32.93%	4.62	2.03%	29.47%	6.061	-40.900
A18789-8	681	258.06	3.63	3.01%	47.42%	4.90	2.31%	32.01%	5.09	2.11%	28.15%	5.565	-9.062

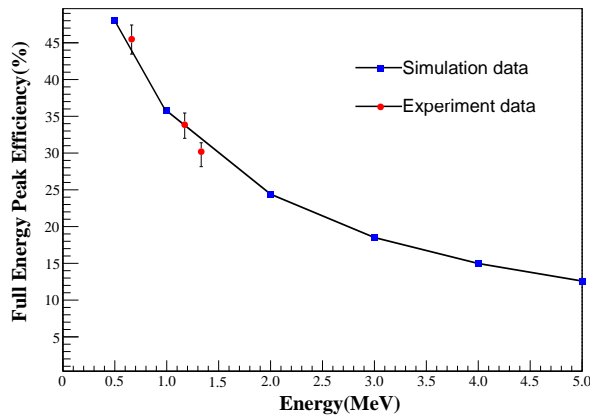


Fig. 13. Comparison between experimental data using the ⁶⁰Co and ¹³⁷Cs sources and simulation (see legend) for the full energy peak efficiency. The solid line connecting the simulation data is used to guide the eyes.

energy spectra of ¹³⁷Cs are shown in Fig. 14(a). Energy depositions from Compton back-scattered events as sharp edges were observed in the simulation plot, and events beyond that edge corresponded to multiple Compton scattering. In an experiment, the sharp Compton edge became smeared owing to the resolution effect. The simulation energy spectra of the ¹³⁷Cs and ⁶⁰Co sources were broadened using Gaussian sampling to match the EJ301 detector resolution. The energy calibration factors were obtained by comparing the experimental energy spectra with the simulated energy spectra after broadening. A comparison of the results is presented in Fig. 14(a). For the neutron detection efficiency of EJ301, a ²⁵²Cf neutron source with an initial activity of 0.1531 μCi, which had a continuous neutron spectrum, was used. The ²⁵²Cf source generally includes both alpha and spontaneous fission (SF) decay branches, with alpha decay comprising 96.91% of the activity and SF comprising the remaining 3.09% with neutron yield, which was approximately 4.4×10^3 neutrons per second per μCi[52]. Neutrons and γ-rays were discriminated using the PSD. The neutron detection efficiency was measured at different high PMT voltages, as shown in Fig. 14(c). For comparison, we simulated the neutron emission of the ²⁵²Cf source. The neutron spectrum was parameterized according

to the following Maxwellian distribution[53]:

$$N(E) = 2\sqrt{\frac{E}{\pi}} T^{3/2} e^{-E/T} \quad (1)$$

where $N(E)$ denotes the number of neutrons with energy E at a nuclear temperature of $T = 1.466$ MeV. The simulated energy spectra obtained using this expression are shown in Fig. 14(b), and the efficiency was approximately 18%. This result was almost in agreement with the efficiency measured at the recommended high voltage of 1625 V.

C. Pulse shape discrimination

The EJ301 liquid scintillator detector was selected for neutron detection as part of the SLEGS TOF spectrometer owing to its excellent PSD properties and fast timing performance. Because organic scintillators are sensitive to γ-rays and neutrons, the pulse shape discrimination (PSD) capability between neutrons and γ-rays was a critical feature that originated from three different components of scintillation light, with mean decay times of 3.16 ns, 32.3 ns, and 270 ns[54, 55]. Different complex PSD methods have been reported, where the charge comparison (CC) method[57] based on the work of Jordanov and Knoll[56] and the zero-crossing method[58] are the most popular. In this section, the CC method, which is based on a comparison between the integrations of signals over two different intervals (entire pulse and only the tail) and the ratio of these two integrations as a separation parameter, was used to estimate EJ301 PSD performance. The following three critical parameters were written in firmware registers: PreGate, which determined the time before the pulse started to integrate, ShortGate, which determined the duration of the integration of the tail, and LongGate, which determined the total integration of the entire pulse. Therefore, PSD was introduced as a parameter for the implementation of the CC method, which is defined by the following equation:

$$PSD = \frac{Q_{\text{long}} - Q_{\text{short}}}{Q_{\text{long}}} \quad (2)$$

$Q_{\text{long}} - Q_{\text{short}}$ corresponds to the integral of the tail, whereas Q_{long} and Q_{short} correspond to the integrals of the total pulse and Short Gate, respectively. Figure 15 shows the PSD spectrum of the ²⁵²Cf radioactive source measured using the

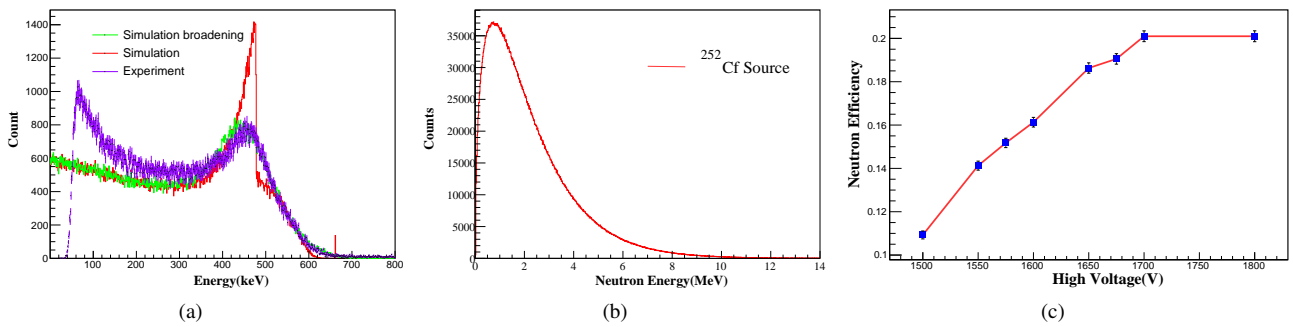


Fig. 14. (Color online) (a) Energy spectra of ^{137}Cs source after calibration, initial spectrum, and Gaussian broadened spectrum based on simulation. (b) Simulated energy spectrum of ^{252}Cf neutron source. (c) Neutron detection efficiency of EJ301 demonstrated using figure-of-merit(FOM) to select neutrons under different high PMT voltages. The solid line connecting the experimental data is used to guide the eyes.

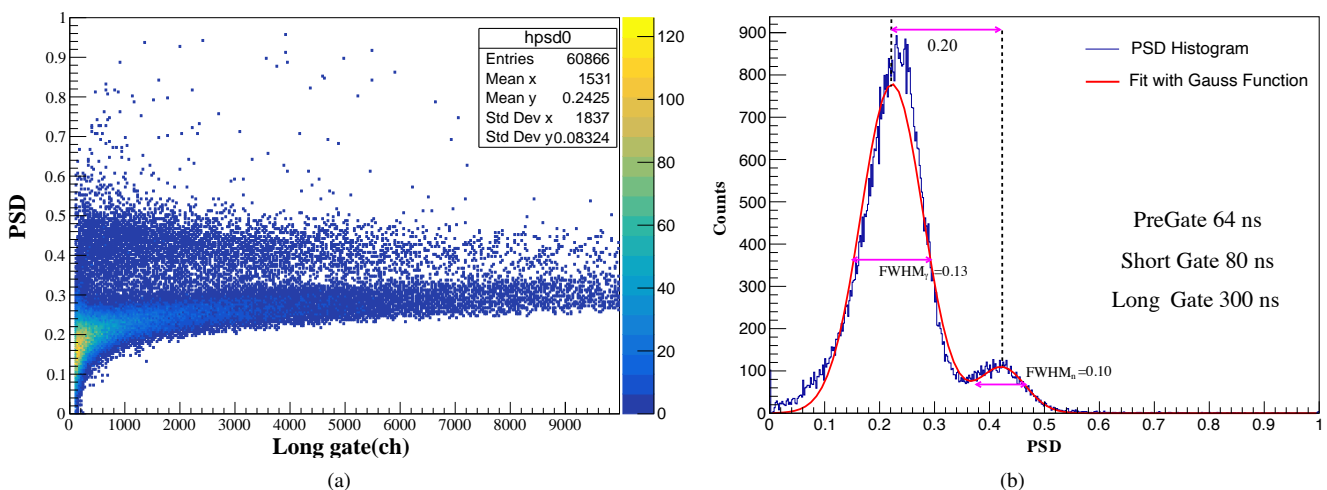


Fig. 15. (Color online) (a) 2D PSD spectrum of the ^{252}Cf radioactive source measured using the EJ301 detector, which was 100 cm from the source. (b) PSD histogram fitted using a double Gaussian function. The FWHMs and distance between γ -ray and neutron peaks are marked. The FOM was equal to 0.6982.

EJ301 detector. Pulses of neutrons generally have longer tails than those of γ -rays, resulting in a larger PSD. Two distinct peaks were formed on both sides of the PSD, corresponding to γ -rays and neutrons. Another crucial parameter was the figure-of-merit (FOM), which represents the resolution of neutrons and γ -rays, as defined by

$$FOM = \frac{S}{FWHM_n + FWHM_{\gamma}} \quad (3)$$

where S is the separation between the peaks shown above, $FWHM_{\gamma}$ is the full-width half-maximum of the spread of events classified as γ -rays, and $FWHM_n$ is the neutron peak. Some optimal setting parameters were necessary for high quality discrimination. Therefore, the effects of the Short Gate, Long Gate, Threshold, and high voltage were evaluated, and the FOMs calculated under different conditions are shown in Fig. 16. The high voltage and threshold

mainly affected the detection efficiency rather than the FOM, whereas the Short Gate of 18 ns and Long Gate of 200 ns were more appropriate for γ/n discrimination.

D. Time resolution

TOF technology was used to measure the fast neutron energies. The time signal of the LaBr_3 detectors or laser was used as the starting time and the time signal of the EJ301 detectors was used as the stopping time. Therefore, the time resolution of the detectors directly determined the accuracy of neutron energy measurements.

For the time resolution of the LaBr_3 detectors, a pair of similar LaBr_3 detectors performed the γ -rays from the ^{252}Cf source coincidentally. Additionally, a time resolution of 20 \times LaBr_3 was studied in [23], which showed that single de-

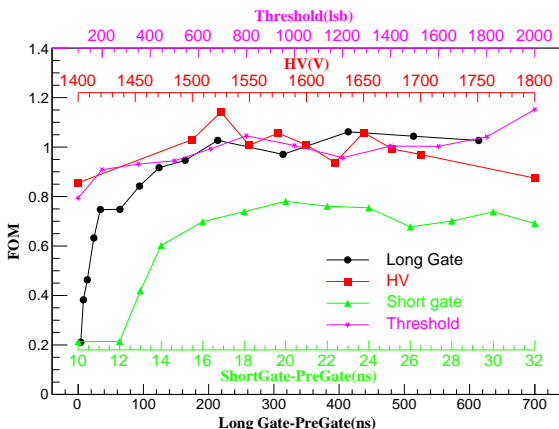


Fig. 16. (Color online) FOMs calculated under different conditions. It should be noted that the integration gates started from a PreGate, and LSB was the least significant bit, which was converted to volt ($1 \text{ LSB} = (\text{input dynamic range in Vpp}) / 2^{N\text{bit}}$). Here, $1 \text{ LSB} = 0.12 \text{ mV}$. The solid lines connecting the experimental data were used to guide the eyes.

tectors almost have similar time resolution. The coincidence time spectrum is shown in Fig. 17(a). The total FWHM was 1.28 ns. According to equation $\Delta T_{\text{exp}}^2 = \Delta T_{\text{LaBr}_3 1}^2 + \Delta T_{\text{LaBr}_3 2}^2$, assuming two detectors have similar performance, time resolution of a single LaBr_3 was 0.90 ns.

Similarly, a coincidence was observed between LaBr_3 and EJ301. To make the time resolution more reasonable, we sliced the long gate integration interval to 100 ch, and the experimental time resolution of each interval is shown in Fig. 17(b). The uncertainty was taken as the root-mean-square (RMS). The average time resolutions for the 30 and 100 cm distances were 1.3 and 1.2 ns, respectively, and these contributions were from LaBr_3 and EJ301. Considering that the time resolution of the LaBr_3 detector was 0.9 ns, the time resolutions of the EJ301 detector were 0.94 ns and 0.79 ns for distances of SI30 and SI100 cm, respectively. The resulting timing uncertainties were significantly smaller than the distance uncertainties of 2.43%, 1.64%, and 1.23% for

100, 150, and 200 cm distances, respectively. For example, for 1 MeV neutrons detected by EJ301 placed at 150 cm, the flight time was approximately 110 ns. The time resolution of the EJ301 detector was 0.94 ns, that is, an error of only 0.8%.

IV. CONCLUSION

This study demonstrated that γ -rays cover the vast majority of induced background, which cannot be absorbed by shielding. Therefore, a thinner target is preferable for reducing the induced background. Fortunately, regardless of the thickness of the target, the background-free signals of GDR decaying to the ground state and neutron signals of interest can be easily separated using appropriate time gate, PSD restriction conditions, and coincidence owing to the excellent time and energy resolution of detectors as well as γ/n discrimination.

In conclusion, the apparatus demonstrated exceptionally good performance in collecting and distinguishing γ -rays and neutrons of GDR decay. This will broaden our understanding of nuclear structures and lead to progress in the measurement of photon-neutron nuclear reactions.

AUTHOR CONTRIBUTIONS

All authors contributed to the study conception and design. Material preparation, data collection and analysis were performed by Kai-Jie Chen, Long-Xiang Liu and Zi-Rui Hao. The first draft of the manuscript was written by Kai-Jie Chen and Hong-Wei Wang, and all authors commented on previous versions of the manuscript. All authors read and approved the final manuscript.

DATA AVAILABILITY STATEMENT

The data that support the findings of this study are openly available in Science Data Bank at <https://www.doi.org/10.57760/sciedb.07467> and <http://resolve.pid21.cn/31253.11.sciedb.07467>.

-
- [1] M.H. Jiang, X. Yang, and H.J. Xu *et al.*, Shanghai Synchrotron Radiation Facility. Chinese Sci. Bull. **54**, 4171-4181 (2009). doi: [10.1007/s11434-009-0689-y](https://doi.org/10.1007/s11434-009-0689-y)
 - [2] Q.Y. Pan, W. Xu, W. Luo *et al.*, A Future Laser Compton Scattering (LCS) γ -Ray Source: SLEGS at SSRF. Synchrotron Radiation News **22**, 11-20 (2009). doi: [10.1080/08940880902959759](https://doi.org/10.1080/08940880902959759)
 - [3] H.W. Wang, G.T. Fan, L.X. Liu *et al.*, Development and prospect of Shanghai laser Compton scattering gamma source. Nucl. Phys. Rev. **37**, 53-63 (2020). doi: [10.11804/NuclPhysRev.37.2019043](https://doi.org/10.11804/NuclPhysRev.37.2019043)
 - [4] H. Xu, G. Fan, H. Wang *et al.*, Interaction chamber for laser Compton slant-scattering in SLEGS beamline at Shanghai Light Source, Nucl. Instrum. Methods Phys. Res. A **1033**, 166742 (2022). doi: [10.1016/j.nima.2022.166742](https://doi.org/10.1016/j.nima.2022.166742)
 - [5] Z.R. Hao, G.T. Fan, H.W. Wang *et al.*, Collimator system of SLEGS beamline at Shanghai Light Source. Nucl. Instrum. Methods Phys. Res. A **1013**, 165638 (2021). doi: [10.1016/j.nima.2021.165638](https://doi.org/10.1016/j.nima.2021.165638)
 - [6] Z.R. Hao, G.T. Fan, H.W. Wang *et al.*, New annular collimator system of SLEGS beamline at Shanghai Light Source. Nucl. Instrum. Methods Phys. Res. B **519**, 9-14 (2022). doi: [10.1016/j.nimb.2022.02.010](https://doi.org/10.1016/j.nimb.2022.02.010)
 - [7] H.W. Wang, G.T. Fan, L. X. Liu *et al.*, commissioning of laser electron gamma beamline SLEGS at SSRF. Nucl. Sci. Tech. **33**, 87 (2022). doi: [10.1007/s41365-022-01076-0](https://doi.org/10.1007/s41365-022-01076-0)
 - [8] A. Zilges, D.L. Balabanski, J. Isaak *et al.*, Photonuclear reactions: From basic research to applications. Progress

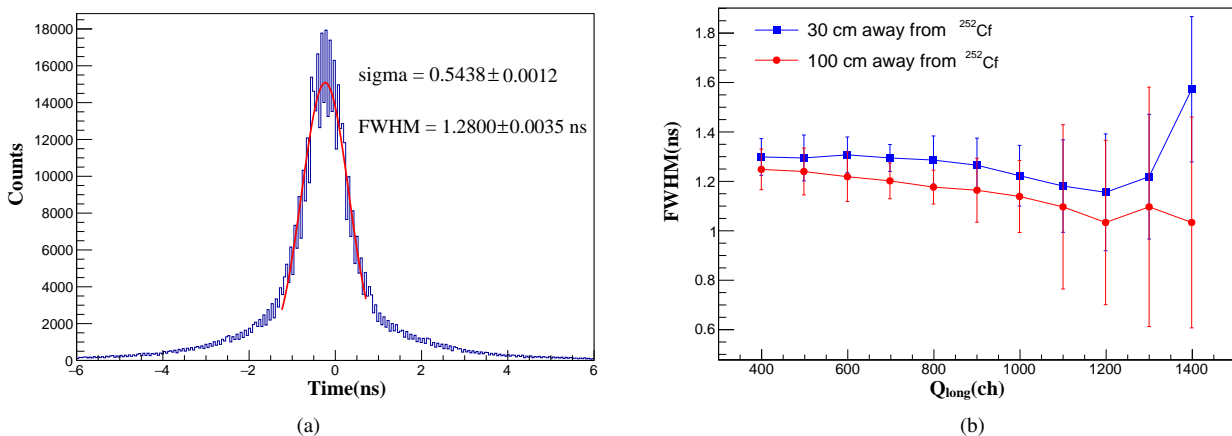


Fig. 17. (a) Two LaBr₃ time spectra measured using γ -rays from ^{252}Cf . Similar time spectra were accomplished for LaBr₃ and an EJ301 detectors. (b) FWHM of time as a function of Q_{long} . The solid lines connecting the experimental data are used to guide the eyes.

- in particle and Nucl. Phys. **122**, 103903 (2022). doi: [10.1016/j.ppnp.2021.103903](https://doi.org/10.1016/j.ppnp.2021.103903)
- [9] J.G. Chen, W. Xu, H.W. Wang *et al.*, Transmutation of nuclear wastes using photonuclear reactions triggered by Compton backscattering photons at the Shanghai laser electron gamma source. Chinese Phys. C **32**, 677-680 (2008). doi: [10.1088/1674-1137/32/8/019](https://doi.org/10.1088/1674-1137/32/8/019)
- [10] D.J.S. Findlay, Applications of photonuclear reactions. Nucl. Instrum. Methods Phys. Res. B **50**, 314-320(1990). doi: [10.1016/0168-583X\(90\)90374-4](https://doi.org/10.1016/0168-583X(90)90374-4)
- [11] Z.R. Hao, G.T. Fan, L.X. Liu *et al.*, Design and simulation of a 4π flat efficiency ^3He neutron detector array. Nucl. Tech. **43**, 110501-110501 (2020). doi: [10.11889/j.0253-3219.2020.hjs.43.110501](https://doi.org/10.11889/j.0253-3219.2020.hjs.43.110501)
- [12] B.L. Berman, S.C. Fultz, Measurements of giant dipole resonance with monoenergetic photons. Rev. Mod. Phys. **47**, 713-761 (1975). doi: [10.1103/RevModPhys.47.713](https://doi.org/10.1103/RevModPhys.47.713)
- [13] B.L. Berman, J.T. Caldwell, R.R. Harvey *et al.*, Photoneutron cross sections for ^{90}Zr , ^{91}Zr , ^{92}Zr , ^{94}Zr , and ^{89}Y . Phys. Rev. **162**, 1098-1111 (1967). doi: [10.1103/PhysRev.162.1098](https://doi.org/10.1103/PhysRev.162.1098)
- [14] H. Utsunomiya, I. Gheorghe, D.M. Filipescu *et al.*, Direct neutron multiplicity sorting with a flat-efficiency detector. Nucl. Instrum. Methods Phys. Res. A **871**, 135-141 (2017). doi: [10.1016/j.nima.2017.08.001](https://doi.org/10.1016/j.nima.2017.08.001)
- [15] X.R. Hu, G.T. Fan, W. Jiang *et al.*, Measurements of the ^{197}Au (n, γ) cross-section up to 100 keV at the CSNS Back-n facility, Nucl. Sci. Tech. **32**, 101 (2021). doi: [10.1007/s41365-021-00931-w](https://doi.org/10.1007/s41365-021-00931-w)
- [16] P. Hu, Z.G. Ma, K. Zhao *et al.*, Development of gated fiber detectors for laser-induced strong electromagnetic pulse environments, Nucl. Sci. Tech. **32**, 58 (2021). doi: [10.1007/s41365-021-00898-8](https://doi.org/10.1007/s41365-021-00898-8)
- [17] J.Y. Tang, Q. An, J.B. Bai *et al.*, Back-n white neutron source at CSNS and its applications, Nucl. Sci. Tech. **32**, 11 (2021). doi: [10.1007/s41365-021-00846-6](https://doi.org/10.1007/s41365-021-00846-6)
- [18] W.B. He, Y.G. Ma, X.G. Cao *et al.*, Giant Dipole Resonance as a fingerprint of α clustering configurations in ^{12}C and ^{16}O , Phys. Rev. Lett. **113**, 032506 (2014). doi: [10.1103/PhysRevLett.113.032506](https://doi.org/10.1103/PhysRevLett.113.032506)
- [19] W.B. He, Y.G. Ma, X.G. Cao *et al.*, Dipole oscillation modes in light α -clustering nuclei, Phys. Rev. C **94**, 014301 (2016). doi: [10.1103/PhysRevC.94.014301](https://doi.org/10.1103/PhysRevC.94.014301)
- [20] B.S. Huang, Y.G. Ma, Dipole excitation of ^6Li and ^9Be studied with an extended quantum molecular dynamics model, Phys. Rev. C **103**, 054318 (2021). doi: [10.1103/PhysRevC.103.054318](https://doi.org/10.1103/PhysRevC.103.054318)
- [21] H. Yakut, E. Tabar, E. Kemah *et al.*, Theoretical description of pygmy and giant dipole resonances in Np-237. Phys. Scripta. **96**, 125315 (2021). doi: [10.1088/1402-4896/ac35c4](https://doi.org/10.1088/1402-4896/ac35c4)
- [22] J.R. Beene, F.E. Bertrand, M.L. Halbert *et al.*, Heavy-ion excitation and photon decay of giant resonances in Pb-208. Phys. Rev. C **39**, 1307-1319 (1989). doi: [10.1103/PhysRevC.39.1307](https://doi.org/10.1103/PhysRevC.39.1307)
- [23] P.A. Söderström, E. Açıksöz, D. L. Balabanski *et al.*, ELIGANT-GN — ELI Gamma Above Neutron Threshold: The Gamma-Neutron setup. Nucl. Instrum. Methods Phys. Res. A **1027**, 166171 (2022). doi: [10.1016/j.nima.2021.166171](https://doi.org/10.1016/j.nima.2021.166171)
- [24] L. Capponi, G. Ciocan, E. Aciksoz *et al.*, Implementation of the ELIGANT neutron and gamma detector arrays at ELI-NP. J. Phys. Conf. Ser. **1643**, 012118 (2020). doi: [10.1088/1742-6596/1643/1/012118](https://doi.org/10.1088/1742-6596/1643/1/012118)
- [25] S. Agostinelli, J. Allison, K. Amako *et al.*, Geant4—a simulation toolkit. Nucl. Instrum. Methods Phys. Res. A **506**, 250-303 (2003). doi: [10.1016/S0168-9002\(03\)01368-8](https://doi.org/10.1016/S0168-9002(03)01368-8)
- [26] A. Giaz, L. Pellegrini, S. Riboldi *et al.*, Characterization of large volume $3.5'' \times 8''$ LaBr₃:Ce detectors. Nucl. Instrum. Methods Phys. Res. A **729**, 910-921 (2013). doi: [10.1016/j.nima.2013.07.084](https://doi.org/10.1016/j.nima.2013.07.084)
- [27] Y.T. Li, W.P. Lin, B.S. Gao *et al.*, Development of a low-background neutron detector array. Nucl. Sci. Tech. **33**, 41 (2022). doi: [10.1007/s41365-022-01030-0](https://doi.org/10.1007/s41365-022-01030-0)
- [28] X.F. Jiang, J.R. Zhou, H. Luo *et al.*, a large-area ^3He tube array detector with vacuum operation capacity for the SANS instrument at the CSNS, Nucl. Sci. Tech. **33**, 89 (2022). doi: [10.1007/s41365-022-01067-1](https://doi.org/10.1007/s41365-022-01067-1)
- [29] H. Cheng, B.H. Sun, L.H. Zhu *et al.*, Intrinsic background radiation of a LaBr₃(Ce) detector via coincidence measurements and simulations, Nucl. Sci. Tech. **31**, 10 (2020). doi: [10.1007/s41365-020-00812-8](https://doi.org/10.1007/s41365-020-00812-8)
- [30] W. Lu, Y. Yuan, T. Zhang *et al.*, Monte Carlo simulation for the performance evaluation of a detector model with a monolithic LaBr₃(Ce) crystal and SiPM array for gamma radiation imaging, Nucl. Sci. Tech. **33**, 107 (2022). doi: [10.1007/s41365-022-01071-9](https://doi.org/10.1007/s41365-022-01071-9)

01081-3

- [31] G. Jaworski, M. Palacz, J. Nyberg *et al.*, Monte Carlo simulation of a single detector unit for the neutron detector array NEDA. Nucl. Instrum. Methods Phys. Res. A **673**, 64-72 (2012). doi: [10.1016/j.nima.2012.01.017](https://doi.org/10.1016/j.nima.2012.01.017)
- [32] M. Krzysiek, F. Camera, D. M. Filipescu *et al.*, Simulation of ELIGANT-GN array performances at ELI-NP for gamma beam energies larger than the neutron threshold. Nucl. Instrum. Methods Phys. Res. A **916**, 257-274 (2019). doi: [10.1016/j.nima.2018.11.058](https://doi.org/10.1016/j.nima.2018.11.058)
- [33] V. Paticchio, G. Derasmo, E. M. Fiore *et al.*, Efficiency measurements of Large Volume Organic Scintillator counters to neutrons of energy from 54 to 360 MeV. Nucl. Instrum. Methods Phys. Res. A **305**, 150-157 (1991). doi: [10.1016/0168-9002\(91\)90528-X](https://doi.org/10.1016/0168-9002(91)90528-X)
- [34] D. Zhao, S. Feng, C. Hu *et al.*, Characterization of neutron/gamma-ray discrimination performance in an EJ-301 liquid scintillator for application to prompt fission neutron spectrum measurements at CSNS. Radiat. Meas. **151**, 106703 (2022). doi: [10.1016/j.radmeas.2022.106703](https://doi.org/10.1016/j.radmeas.2022.106703)
- [35] J. Qin, C. Lai, and B. Ye *et al.*, Characterization of BC501A and BC537 liquid scintillator detectors. Appl. Radiat. Isot. **104**, 15-24 (2015). doi: [10.1016/j.apradiso.2015.06.008](https://doi.org/10.1016/j.apradiso.2015.06.008)
- [36] D.A. Brown, M.B. Chadwick, R. Capote *et al.*, ENDF/B-VIII.0: The 8th Major Release of the nuclear reaction data library with CIELO-project cross-sections, new standards, and thermal scattering data. Nucl. Data Sheets **148**, 1-142 (2018). doi: [10.1016/j.nds.2018.02.001](https://doi.org/10.1016/j.nds.2018.02.001)
- [37] S.Y. Chang, Z.H. Wang, Y.F. Niu *et al.*, Relativistic random-phase approximation description of M1 excitations with the inclusion of pi mesons. Phys. Rev. C **105**, 034330 (2022). doi: [10.1103/PhysRevC.105.034330](https://doi.org/10.1103/PhysRevC.105.034330)
- [38] N. Ryezayeva, T. Hartmann, Y. Kalmykov *et al.*, Nature of low-energy dipole strength in nuclei: The case of a resonance at particle threshold in Pb-208. Phys. Rev. Lett. **89**, 272502 (2002). doi: [10.1103/PhysRevLett.89.272502](https://doi.org/10.1103/PhysRevLett.89.272502)
- [39] Y. Xu, S. Goriely, E. Khan, Systematic studies of E1 photon strength functions combining the Skyrme-Hartree-Fock-Bogoliubov plus quasiparticle random-phase approximation model and experimental giant dipole resonance properties. Phys. Rev. C **104**, 044301 (2021). doi: [10.1103/PhysRevC.104.044301](https://doi.org/10.1103/PhysRevC.104.044301)
- [40] H. Ozdogan, M. Sekerci, A. Kaplan, Photoneutron cross-section calculations of ^{54}Fe , ^{56}Fe , ^{90}Zr , ^{91}Zr , ^{92}Zr , ^{94}Zr , ^{93}Nb , and ^{107}Ag isotopes with newly obtained Giant Dipole Resonance parameters. Appl. Radiat. Isot. **165**, 109356 (2020). doi: [10.1016/j.apradiso.2020.109356](https://doi.org/10.1016/j.apradiso.2020.109356)
- [41] N.F. Lattoofi and A. A. Alzubadi, AA. Study of giant dipole resonances for Nd isotopes with an exciton model. Int. J. Mod. Phys. E **29**, 2050084 (2020). doi: [10.1142/S0218301320500846](https://doi.org/10.1142/S0218301320500846)
- [42] CAEN S.p.A., N1470 Programmable HV Power Supply. (CAEN 2021), <https://www.caen.it/products/n1470/>. Accessed 06 Feb 2022
- [43] W-IE-NE-R Power Electronics Group and W-IE-NE-R Power Electronics GMBH, NIM CAMAC Crates. (W-IE-NE-R, 2021) https://file.wiener-d.com/documentation/NIM-CAMAC/WIENER_NIM-CAMAC-Crates_Manual_A3.pdf. Accessed 06 Feb 2022
- [44] CAEN S.p.A., A7030-AG7030 3kV/ 1mA (1.5W) HV board. (CAEN, 2019) <https://www.caen.it/products/a7030/>. Accessed 06 Feb 2022
- [45] CAEN S.p.A. SY5527/SY5527LC Universal Multichannel Power Supply Systems 6/4 slots Mainframes. (CAEN, 2022) <https://www.caen.it/products/sy5527lc/>. Accessed 06 Feb 2022
- [46] CAEN S.p.A. User manual UM2792 V1730/VX1730 and V1725/VX1725 waveform Digitizer. (CAEN, 2021) <https://www.caen.it/products/v1730/>. Accessed 06 Feb 2022
- [47] CAEN S.p.A. A3818 PCI Express Optical Link. (CAEN, 2020) <https://www.caen.it/products/a3818/>. Accessed 06 Feb 2022
- [48] A. Nassalski, M. Moszynski, A. Syntfeld-Kazuch *et al.*, Non-proportionality of organic scintillators and BGO. IEEE Trans. Nucl. Sci. **55**, 1069-1072 (2008). doi: [10.1109/Tns.2007.913478](https://doi.org/10.1109/Tns.2007.913478)
- [49] Z.S. Hartwig, P. Gumplinger, Simulating response functions and pulse shape discrimination for organic scintillation detectors with Geant4. Nucl. Instrum. Methods Phys. Res. A **737**, 155-162 (2014). doi: [10.1016/j.nima.2013.11.027](https://doi.org/10.1016/j.nima.2013.11.027)
- [50] Y.P. Xu, G. Randers-Pehrson, S.A. Marino *et al.*, Broad energy range neutron spectroscopy using a liquid scintillator and a proportional counter: Application to a neutron spectrum similar to that of an improvised nuclear device. Nucl. Instrum. Methods Phys. Res. A **794**, 234-239 (2015). doi: [10.1016/j.nima.2015.05.041](https://doi.org/10.1016/j.nima.2015.05.041)
- [51] R. Batchelor, W.B. Gilboy, J.B. Parker *et al.*, The response of organic scintillators to fast neutrons. Nucl. Instrum. Methods **13**, 70-82 (1961). doi: [10.1016/0029-554X\(61\)90171-9](https://doi.org/10.1016/0029-554X(61)90171-9)
- [52] A.M. Mattera, S. Zhu, A.B. Hayes *et al.*, Nucl. The data Sheets for A252. Nucl. Data Sheets **172**, 543-587 (2021). doi: [10.1016/j.nds.2021.02.002](https://doi.org/10.1016/j.nds.2021.02.002)
- [53] J. Csikai, Z. Dezsö, Fission neutron spectrum of ^{252}Cf . Ann. Nucl. Energy **3**, 527-530 (1976). doi: [10.1016/0306-4549\(76\)90068-2](https://doi.org/10.1016/0306-4549(76)90068-2)
- [54] F.T. Kuchnir, F.J. Lynch, Time dependence of scintillations and the effect on pulse-shape discrimination. IEEE Trans. Nucl. Sci. **15**, 107-113 (1968). doi: [10.1109/tns.1968.4324923](https://doi.org/10.1109/tns.1968.4324923)
- [55] ELJEN Technology, EJ-301 Liquid Scintillator(Eljen Technology, 2017) https://eljentechnology.com/images/products/data_sheets/EJ-301_EJ-309.pdf. Accessed 06 Feb 2022
- [56] V.T. Jordanov, G.F. Knoll, Digital synthesis of pulse shapes in real-time for high-resolution radiation spectroscopy. Nucl. Instrum. Methods Phys. Res. A **345**, 337-345 (1994). doi: [10.1016/0168-9002\(94\)91011-1](https://doi.org/10.1016/0168-9002(94)91011-1)
- [57] T.K. Alexander, F.S. Goulding, An amplitude-insensitive system that distinguishes pulses of different shapes. Nucl. Instrum. Methods **13**, 244-246 (1961). doi: [10.1016/0029-554X\(61\)90198-7](https://doi.org/10.1016/0029-554X(61)90198-7)
- [58] S. Normand, B. Mouanda, S. Haan *et al.*, Discrimination methods between neutron and gamma rays for boron-loaded plastic scintillators. Nucl. Instrum. Methods Phys. Res. A **484**, 342-350 (2002). doi: [10.1016/S0168-9002\(01\)02016-2](https://doi.org/10.1016/S0168-9002(01)02016-2)